
# Molecular structure, binding, and disorder in TDBC-Ag plexcitonic assemblies

RESEARCH ARTICLE | JULY 01 2026

# Molecular structure, binding, and disorder in TDBC–Ag plexcitonic assemblies

**Special Collection:** Festschrift in honor of Jianshu Cao: Non-equilibrium kinetics and quantum dynamics

J. Baños-Gutiérrez ; R. Bercy ; Y. García Jomaso ; S. Balci ; G. Pirruccio ; J. Halldin Stenlid ; M. J. Llansola-Portoles ; D. Finkelstein-Shapiro



*J. Chem. Phys.* 165, 014702 (2026)
https://doi.org/10.1063/5.0325564

The Journal of Chemical Physics ARTICLE pubs.aip.org/aip/jcp

# Molecular structure, binding, and disorder in TDBC–Ag plexcitonic assemblies

Cite as: J. Chem. Phys. 165, 014702 (2026); doi: 10.1063/5.0325564
Submitted: 31 January 2026 • Accepted: 10 June 2026 •
Published Online: 1 July 2026



J. Baños-Gutiérrez,[1] R. Bercy,[2] Y. García Jomaso,[3] S. Balci,[4] G. Pirruccio,[3] J. Halldin Stenlid,[5] M. J. Llansola-Portoles,[2] and D. Finkelstein-Shapiro[1,a)]

## AFFILIATIONS

[1] Instituto de Quimica, Universidad Nacional Autonoma de Mexico, Circuito Exterior, Ciudad Universitaria, Alcaldía Coyoacán C.P., 04510 Ciudad de Mexico, Mexico
[2] Université Paris-Saclay, CEA, CNRS, Institute for Integrative Biology of the Cell (I2BC), 91198, Gif-sur-Yvette, France
[3] Instituto de Física, Universidad Nacional Autónoma de México, Apartado Postal 20-364, Ciudad de México C.P. 01000, Mexico
[4] Department of Photonics, Izmir Institute of Technology, 35430 Izmir, Turkey
[5] Department of Chemistry and Chemical Engineering, Chalmers University of Technology, Kemivägen 10, SE-412 96 Gothenburg, Sweden

**Note:** This paper is part of the Special Topic Festschrift in Honor of Jianshu Cao: Non-Equilibrium Kinetics and Quantum Dynamics.

[a)] **Author to whom correspondence should be addressed:** daniel.finkelstein@iquimica.unam.mx

## ABSTRACT

Plexcitonic assemblies are hybrid materials composed of a plasmonic nanoparticle and molecular or semiconducting emitters whose electronic transitions are strongly coupled to the plasmonic mode. This coupling hybridizes the system modes into upper and lower polariton branches. The interaction strength depends on the number of emitters and on their orientation and spatial arrangement relative to the metallic surface. These structural factors have profound consequences for the ensuing photoexcited dynamics. Despite the extensive spectroscopic work on plexcitonic systems, direct understanding of the molecular geometry at the metal interface remains limited. We present a comprehensive structural characterization of a model plexciton formed by the cyanine dye 5,5′,6,6′-tetrachloro-1,1′-diethyl-3,3′-di(4-sulfobutyl)-benzimidazolocarbocyanine (TDBC) and silver nanodisks using NMR, THz-Raman spectroscopy, and density functional theory calculations. By comparing the signals from the monomeric and aggregated forms of TDBC with those of the plexciton, we identify shared spectral fingerprints that reveal how molecular packing is modified when the aggregate adsorbs on the silver surface. We observe Raman modes specific to plexciton systems and identify NOESY cross-peaks in the aliphatic region that, along with several Raman modes, are sensitive indicators of aggregation geometry and adsorption. We find that TDBC monomers adopt an asymmetric conformation in which both sulfobutyl chains lie on the same side of the chromophore, while J-aggregates adopt a symmetric up–down alternation of the chains from molecule to molecule, which becomes distorted and loses long range periodicity when adsorbed on Ag nanodisks. This work constrains the molecular geometry and interfacial arrangement of a prototypical TDBC–silver plexciton, providing a structural benchmark for understanding geometry-dependent photophysics in exciton–plasmon systems.



## I. INTRODUCTION

Plexcitons are composed of a plasmonic nanoparticle decorated by semiconducting or molecular emitters whose radiative transition strongly couples to the plasmonic mode and forms hybrid light–matter, or polaritonic, states.[1–7] These states are strongly delocalized and have been proposed for long distance energy transport,[8–11] lasing,[12] and chemical reactivity.[13–15] The orientation and distance between the molecule and the metal influence the strength of the coupling and the energetic landscape in which the ultrafast dynamics occurs. In contrast to the behavior observed in Fabry–Perot based polaritons, where molecules lie in the middle

of the cavity, far away from the mirrors, the molecules in plexcitons exist at the surface of the nanoparticle, opening interfacial charge and energy transfer channels.[16,17] The most promising plexcitonic systems use highly anisotropic nanoparticles such as prisms,[18] urchins,[4,19,20] donuts, and disks,[21] thereby creating a corresponding anisotropy in the metal–molecule coupling.[22]

Disorder plays a nontrivial role in cavity polaritons by mediating the hybridization between bright collective excitations and the dark excitonic manifold. In disordered molecular ensembles, energetic and orientational disorder mixes dark excitons with the cavity-coupled bright mode, thereby reshaping the effective non-Hermitian polaritonic Hamiltonian. Using an exact Green's-function treatment of disordered quantum emitters in multimode cavities, Engelhardt and Cao showed that disorder renormalizes polariton dispersion and produces a crossover from coherent underdamped dynamics to overdamped relaxation as disorder increases.[11] Importantly, this framework demonstrates that dark states actively participate in determining the cavity local density of states and relaxation pathways rather than acting as a passive reservoir. Extending beyond single-mode and one-dimensional models, Sun *et al.* demonstrated that in realistic three-dimensional multimode Fabry–Pérot cavities, dark states can become highly delocalized across hundreds of molecules, with a participation ratio that scales linearly with the number of molecules in the plane parallel to the cavity mirrors, even in the presence of energetic and orientational disorder. Together, these results establish that disorder does not simply localize polaritons but instead controls the extent, geometry, and dimensionality of dark-state delocalization, with direct implications for energy transport, relaxation bottlenecks, and cavity-modified chemistry.[23] A central difficulty in applying these theoretical frameworks to plexcitons is the lack of direct experimental knowledge of molecular geometry and structural disorder. In particular, distinguishing between preserved aggregate packing and adsorption-induced distortion at metal interfaces remains unresolved.

In plexcitonic systems, where molecular excitons hybridize with localized surface plasmon resonances, disorder plays an even more central role due to the intrinsically open, lossy, and spatially inhomogeneous nature of plasmonic nanostructures.[24] Structural disorder in molecular aggregates (e.g., energetic inhomogeneity, finite exciton delocalization length, and polymorphism) coexists with electromagnetic heterogeneity arising from plasmonic mode confinement, retardation, and nanoparticle-to-nanoparticle variability.[4,22] Peruffo *et al.* studied the conformation of porphyrins bound to Au nanoparticles of different sizes under a variety of conditions and concluded that the orientation of the molecule can vary from perpendicular to planar with respect to the surface of the nanoparticle, binding on the metallic surface or via the surface capping ligands.[4,19,20] Unlike cavity polaritons, plexcitons couple molecular excitations to a dominant plasmonic mode and to a continuum of metallic excitations, an interaction that is very sensitive to distance and orientation. Dark excitons can acquire finite plasmonic character through near-field coupling; plasmonic modes other than dipolar can hybridize with bright exciton states,[25] and strictly dark states can influence the dynamics by interfacial energy transfer. Disorder, therefore, strongly affects not only the strength of the exciton–plasmon coupling but also the effective number of molecules contributing to the plexcitonic mode, the emergence of localized vs collective hybrid states, and the creation of dark states that can act as exciton traps. Plexcitonic photophysics reflect a disorder-controlled competition between exciton delocalization, localization imposed by dark states or uncoupled molecules, and quenching due to interfacial processes.

Organic molecular aggregates are an important class of emitters in plexcitonic assemblies.[18,26,27] Depending on the relative angle between the transition dipole moments of its constituents, the aggregates fall into J-aggregates, H-aggregates, or X-aggregates.[28,29] J-aggregates concentrate the individual molecular transition dipole moments into a very bright collective transition that is redshifted with respect to the monomer, with a very large fluorescence quantum yield and a small Stokes' shift.[28] The formation of these structures depends on the intrinsic molecular properties such as $\pi$–$\pi$ interactions, hydrogen bonding, and steric repulsion, as well as the solvent composition, spectator ions, and overall dye concentration.[30] J-aggregates of cyanine dyes can adopt several distinct packing geometries, each defined by how adjacent chromophores laterally slip and stack. Among the most common motifs are staircase and ladder arrangements [Figs. 1(c) and 1(b)], in which molecules form quasi-one-dimensional slip-stacked chains that differ in the direction of slippage relative to the aggregate axis. These chain-like units often act as fundamental building blocks within larger two-dimensional sheets. A third structural motif is the brickwork arrangement [Fig. 1(a)], a two-dimensional packing characterized by larger lateral offsets between neighboring chromophores. Together, these geometries underpin the rich polymorphism observed in J-aggregate morphologies—from narrow fibrils to extended monolayers—and they provide the structural basis for the excitonic coupling that defines the optical response of these materials.[31,32] These structural motifs are often spectroscopically nearly degenerate in the electronic domain, making vibrational or NMR probes essential for their discrimination.

5,5′,6,6′-tetrachloro-1,1′-diethyl-3,3′-di(4-sulfobutyl)-benzimidazolocarbocyanine (TDBC) is one of the workhorses of polaritonic materials due to its large oscillator strength and its well-defined J-aggregate signature (Fig. 2). It is a cyanine dye with a three-carbon bridge between the two benzimidazole rings. Its longest aliphatic chain terminates in sulfonate groups that provide strong attachment on metallic surfaces, which has made it a desirable molecule in plexcitonic systems as well. Bawendi and co-workers recently synthesized a silica-capped TDBC aggregate and, on the basis of the STM-determined molecular layer height, concluded that the

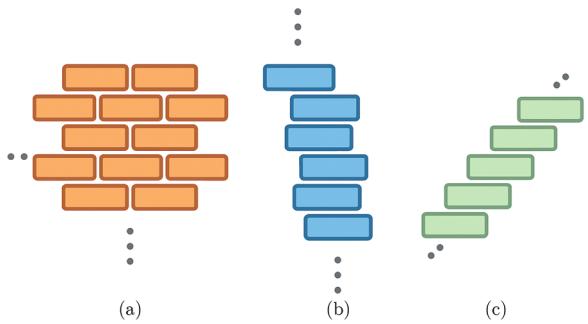


**FIG. 1.** Possible geometries for J-aggregates are (a) brickwork, (b) ladder, and (c) staircase.

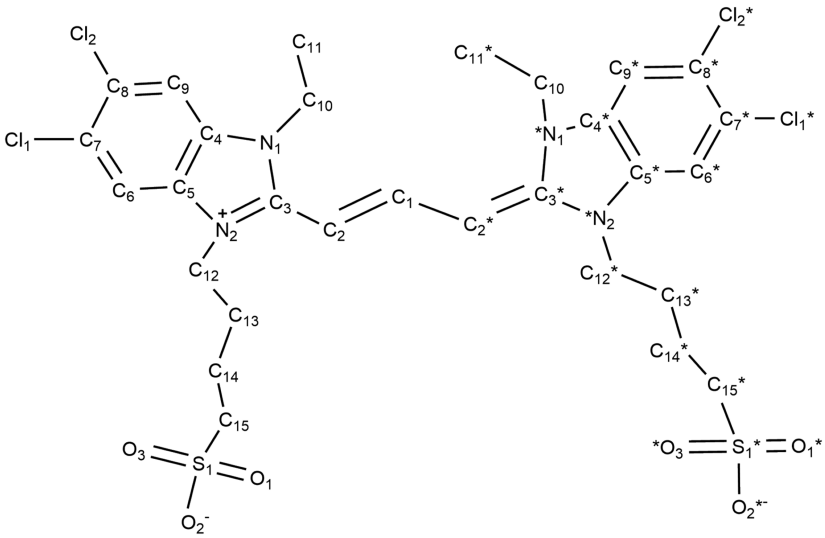


**FIG. 2.** Chemical structure of TDBC. We label only non-equivalent atoms and use the ∗ symbol to denote mirror atoms. We do not show hydrogens explicitly and will refer to them in the text according to the number of the carbon they are attached to.

dye aggregated in a planar arrangement with the dye alternating the orientation of the long aliphatic chains.[33] Coles *et al.* carried out an extensive Raman scattering investigation of TDBC in its monomeric (preferred configuration in methanol) and aggregated (preferred configuration in water) form.[34] By screening a number of conformers with Density Functional Theory (DFT), they were able to suggest the most likely conformers.

In this work, we combine high-field NMR, resonance Raman, and THz-Raman spectroscopy supported by density functional theory to interrogate the molecular structure of TDBC across three distinct regimes: isolated monomers in methanol, J-aggregates in aqueous solution, and Ag-bound plexcitonic assemblies. By directly comparing these reference states, we identify spectroscopic signatures that report on molecular conformation, intermolecular packing, and adsorption-induced distortions at the metal interface. In particular, NOESY cross-peaks provide constraints on side chain symmetry and aggregate packing, while vibrational modes spanning the Raman and THz-Raman regimes selectively probe short-range molecular geometry and longer-range collective order, respectively. Together, these complementary probes allow us to constrain the most probable molecular arrangements in TDBC–Ag plexcitons and to identify experimentally accessible markers of structural heterogeneity relevant for exciton–plasmon hybridization.

## II. METHODS

**Materials**.5,5′,6,6′-tetrachloro-1,1′-diethyl-3,3′-di(4-sulfobutyl)-benzimidazolocarbocyanine (TDBC) was purchased from Few Chemicals. For NMR experiments, the dye was purified following a reported procedure.[33,35] Briefly, TDBC is dissolved in anhydrous methanol, and the solvent is allowed to slowly evaporate until the TDBC concentration exceeds its solubility limit, causing it to precipitate out of solution. Since the impurities are more soluble than TDBC, they remain preferentially in the supernatant, which is discarded before full evaporation. This procedure is repeated two more times to further improve purity. As confirmed by NMR, the relative concentration of impurities decreases from ~30% in the as-received material to trace amounts after purification.

**Aggregate preparation**. For either monomeric or J-aggregates, TDBC was dissolved in either methanol or water, respectively, and sonicated for 5 min prior to use. For resonance Raman measurements, a concentration of 0.5 mg/ml was used, following earlier work.[34] The samples were then placed in a liquid nitrogen bath to avoid radiation damage. For THz-Raman measurements, 2 mg/ml samples were prepared and measured at room temperature in a confocal microscope geometry.

**Synthesis of nanodisks**. Silver and plexcitonic nanodisks were synthesized following previously reported procedures.[18,21,36] First, a seed solution of Ag nanoparticles was prepared by combining 5 ml of 2.5 mM trisodium citrate, 0.25 ml of 500 mg/l poly(sodium 4-styrenesulfonate) (PSS), and 0.3 ml of freshly prepared 10 mM $NaBH_4$. To this mixture, 5 ml of 0.5 mM $AgNO_3$ was added dropwise at ~2 ml/min under vigorous stirring. After 30 min, a yellow colloidal suspension of silver nanoparticles was obtained. For nanoprism growth, 5 ml of Millipore water was combined with 75 $\mu$l of 10 mM ascorbic acid and 60 $\mu$l of the seed solution. Then, 3 ml of 0.5 mM $AgNO_3$ was added dropwise (≈1 ml/min) under vigorous stirring. During this addition, the colloid color evolved from yellow to red and finally to blue, indicating the formation of nanoprisms with a plasmon resonance near 750 nm. The nanoprisms were then stabilized by adding 0.5 ml of 25 mM trisodium citrate. All reactions were carried out in aqueous medium at room temperature using Millipore water throughout. To blueshift the plasmon resonance, the nanoprism suspension was heated in an oil bath at 90 °C for 90 min, after which the resonance wavelength was centered at 600 nm. Finally, the nanodisks were centrifuged at 7000 rpm for 15 min to remove residual seed particles.

**Preparation of plexcitonic assemblies**. Plexcitonic assemblies were prepared by adding 100 $\mu$l of a 0.1 mM TDBC solution per ml of the Ag ND colloid. The mixture was centrifuged for 15 min at 7000 rpm to remove unbound dye, and the resulting precipitate was redispersed in water.

**UV–Vis**. Optical absorption was measured in an Agilent Cary 100 UV–Vis spectrometer in a 1 mm quartz cuvette.

**NMR**. $^1$H NMR was recorded at 298 K on a Bruker 700 MHz AVANCE III HD NMR spectrometer, equipped with a (H–C/N–D)

cryoprobe. TDBC was dissolved in deuterated water at a concentration of 5 mg/ml, in deuterated methanol at a concentration of 2.5 mg/ml, and in a 6:4 (v/v) deuterated methanol–deuterated water solvent mixture at a concentration of 2.5 mg/ml. All samples were sonicated prior to measurement, and no precipitate or scattering was observed.

**Resonance Raman spectra**. Raman spectra above 400 $cm^{-1}$ were recorded using excitation wavelengths of 441 nm (HeCd laser, Liconix), 577 nm (Genesis CX STM, Coherent), and 647 nm (Kr+ laser, Innova 90). The excitation beam was spectrally filtered and focused onto the sample using a lens with a focal length of 50 mm, resulting in an estimated spot size of ~100 $\mu$m at the sample. The incident power was attenuated to below 5 mW to avoid photoinduced effects. The Raman scattering was collected in a backscattering geometry using a second lens (f = 150 mm) and directed into a Jobin-Yvon U1000 double-grating spectrometer equipped with 1800 grooves/mm gratings and a red-sensitive, back-illuminated, liquid-nitrogen-cooled CCD detector. Measurements were performed on samples prepared at 0.5 mg/ml, mounted in a LN2-cooled flow cryostat (Air Liquide, France), and maintained at 77 K to avoid photodegradation. Sample stability was verified by comparing spectra acquired before and after prolonged illumination, and no measurable changes were observed. Baseline subtraction was performed using a polynomial correction.

**THz-Raman spectra**. An excitation beam coming from a HeNe 633 nm laser was spectrally cleaned using an Optigrate Bragg filter and focused onto the sample using a microscope objective lens (NA = 0.9), producing a near diffraction limited spot size of 1 $\mu$m at the sample. The Raman scattering signal was collected with the same excitation objective lens and separated from the Rayleigh signal and residual laser line with three Optigrate notch filters (each filter having an OD >3). The collected light was directed and focused onto an Andor Kymera spectrometer equipped with a 1200 l/mm grating and a TE-cooled iDus CCD camera for detection. Calibration of the THz region was carried out using a solid sulfur sample. Sample stability was confirmed by monitoring the Raman signal as a function of time during prolonged exposure and verifying that no new modes appeared. The THz-Raman spectra were acquired in solution samples at a concentration of 2 mg/ml and room temperature using a microscope slide with a microwell covered with a coverslip to prevent evaporation. Several samples on different days were measured to check reproducibility. The baseline was subtracted using a simple polynomial (uncorrected spectra shown in the supplementary material).

**Computational details**. DFT calculations were carried out in Gaussian 16[37] with the B3LYP functional,[38,39] the def2-SVP basis set[40] with W06 density fitting[41] and with D3(BJ) dispersion corrections[42,43] to account for van der Waals interactions.[40,41] The periodic surface slab calculations were performed in the Vienna *Ab-initio* Simulation Package (VASP)[44–46] using the RPBE functional.[47] The solvent dielectric function was accounted for with a solvent reaction field model (SCRF) using the IEF-PCM method. The frequency of the normal modes was calculated and rescaled by 0.98.[34]

The Raman activities, $S_i$ corresponding to a mode of frequency $\nu_i$, obtained from Gaussian, were transformed into Raman intensities, $I_i^R$, following

$$I_i^R = \frac{C(\nu_i - \nu_0)^4 S_i}{\nu_i\left[1 - \exp\left(-\frac{hc\nu_i}{kT}\right)\right]}, \quad (1)$$

where $c$ is the light speed and $\nu_0$ is the excitation laser frequency. The constant $C$ has a value of $1 \times 10^{-17}$.

Because the experimental spectra are resonance-enhanced whereas the DFT Raman activities correspond to the non-resonant Placzek approximation [Eq. (1)], we primarily use the calculations to guide mode assignment and to interpret frequency shifts and mode character, while relative intensities are discussed only qualitatively. The nuclear displacements defining each normal mode are determined by the ground-state potential energy surface and are, therefore, independent of the resonance condition, making the DFT mode assignments transferable to the resonant regime. The nuclear displacements of the most intense modes appear in the supplementary material.

## III. RESULTS

### A. Synthesis and optical absorption spectroscopy

Silver nanodisks (Ag NDs) were synthesized following previously reported procedures (see Sec. II and Refs. 18, 21, and 36). The resulting colloidal suspension exhibits a plasmonic absorption band centered around 600 nm (Fig. 3). Upon adsorption of TDBC onto the Ag nanodisks, the plasmonic resonance undergoes a clear spectral splitting, consistent with the formation of plexcitonic states (Fig. 3). For comparison, Fig. 3 also shows the absorption spectra of monomeric TDBC in methanol, characterized by a vibronic progression, as well as that of aggregated TDBC in water, which displays the expected redshifted and narrowed absorption band relative to the monomer. These four spectra define the reference electronic environments against which the vibrational and structural signatures discussed below are interpreted.

### B. NMR

**$^1$H NMR**. We recorded the $^1$H spectra of TDBC monomers, J-aggregates, and plexcitons. We found a significant difference between the spectra of TDBC as received or purified following the work of Ref. 35. We report the spectra of the as-received samples in the supplementary material and those of the purified TDBC in the main text. The $^1$H resonances of the monomer in deuterated MeOH are consistent with those previously reported[48] (see Fig. 4 and the supplementary material). In pure $D_2O$, we observe a complete disappearance of the signal, despite the solubility threshold of TDBC in $D_2O$ being higher than in $CD_3OD$ and the absence of increased light scattering indicative of precipitation (Fig. 4). We, therefore, attribute the signal loss to the formation of large, water-soluble aggregates of effective radius $r$ whose rotational correlation time $\tau_c \propto r^3$ (Stokes–Einstein–Debye) places them in the slow-tumbling regime, where transverse relaxation rates scale linearly with $\tau_c$ and the resulting homogeneous broadening renders the resonances undetectable.[49,50] To restrict the aggregate size, we dissolved TDBC in a deuterated 6:4 (v/v) methanol–water mixture. We observe several chemical shift changes as well as a broadening of all peaks indicative of an increased rotational correlation time expected for aggregate species. This is further supported by a change

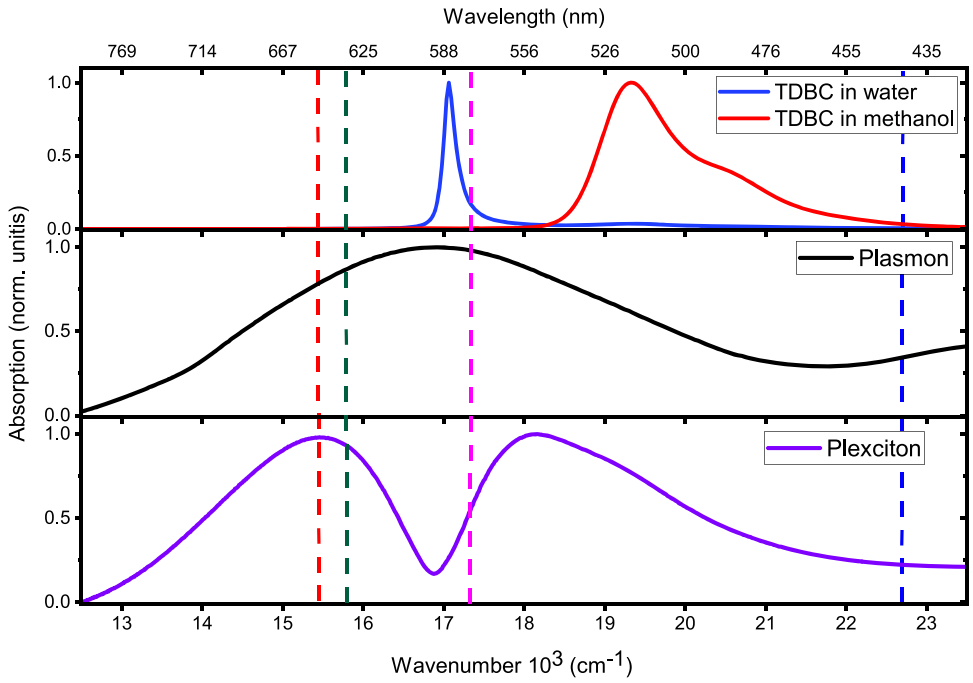


**FIG. 3.** Normalized absorption spectra of TDBC in water (blue), TDBC in methanol (red), Ag nanodisks (black), and the plexciton (purple). Dotted lines indicate the laser excitation wavelengths. For Raman measurements, the red, pink, and blue lines correspond to excitation wavelengths of 647, 577, and 441 nm, respectively, while the green line denotes the THz-Raman excitation wavelength at 633 nm.

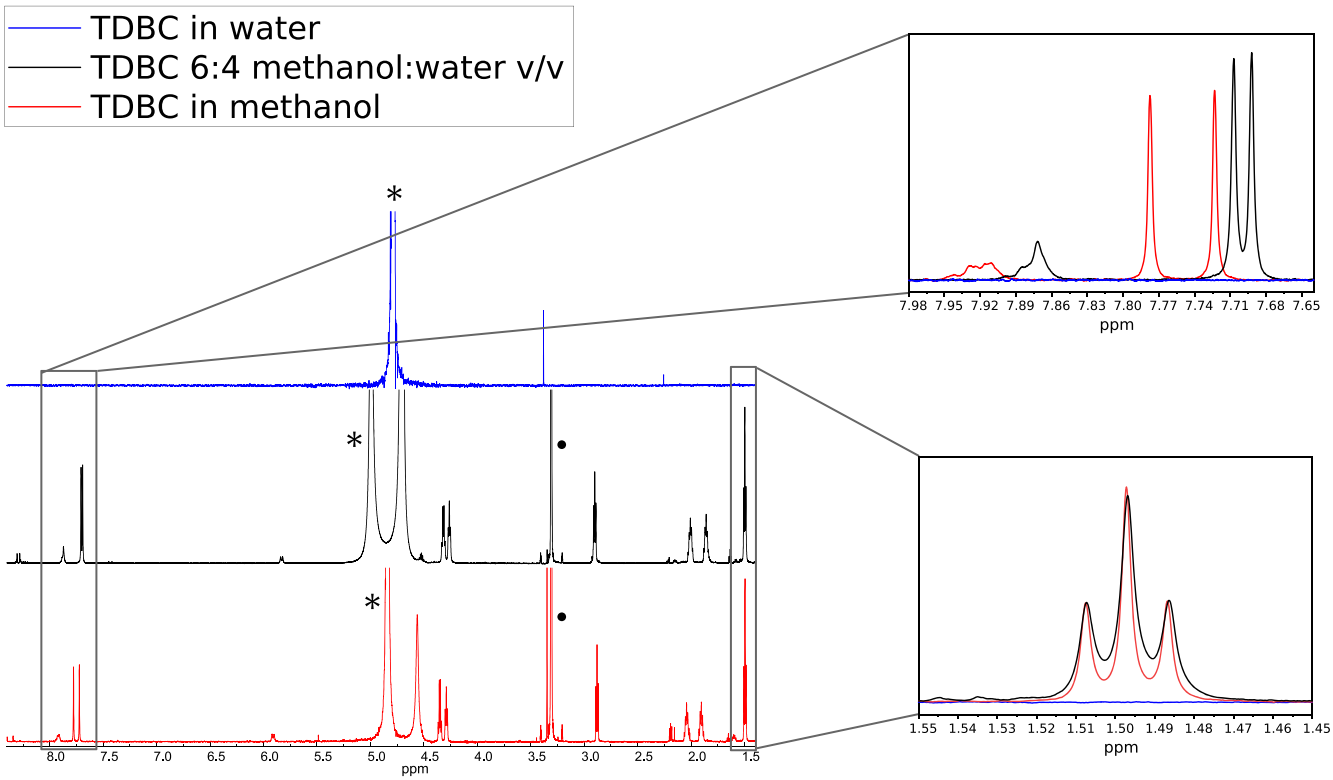


**FIG. 4.** $^{1}$H spectra of TDBC in $CD_3OD$ (red), in a 6:4 (v/v) $CD_3OD$–$D_2O$ mixture (black), and in water (blue). The residual water solvent peak is indicated by an asterisk, while the residual methanol solvent peaks are marked with a circle. The insets show chemical shift changes and aggregation induced broadening.

in the relative sign of the NOESY cross-peaks (see below), which is consistent with the observed signal being representative of the aggregated species. $^{1}$H NMR spectra of plexcitonic assemblies yield a single broadened signal in the aromatic region and a congested set of resonances in the aliphatic region (see the supplementary material).

Owing to the presence of stabilizing ligands on the Ag nanodisks, the expected increase in effective aggregate size in water, and the large hydrodynamic radius of the ND–dye complex, these spectra are dominated by severe line broadening and overlap. As a result, we do not attempt a quantitative structural interpretation of the

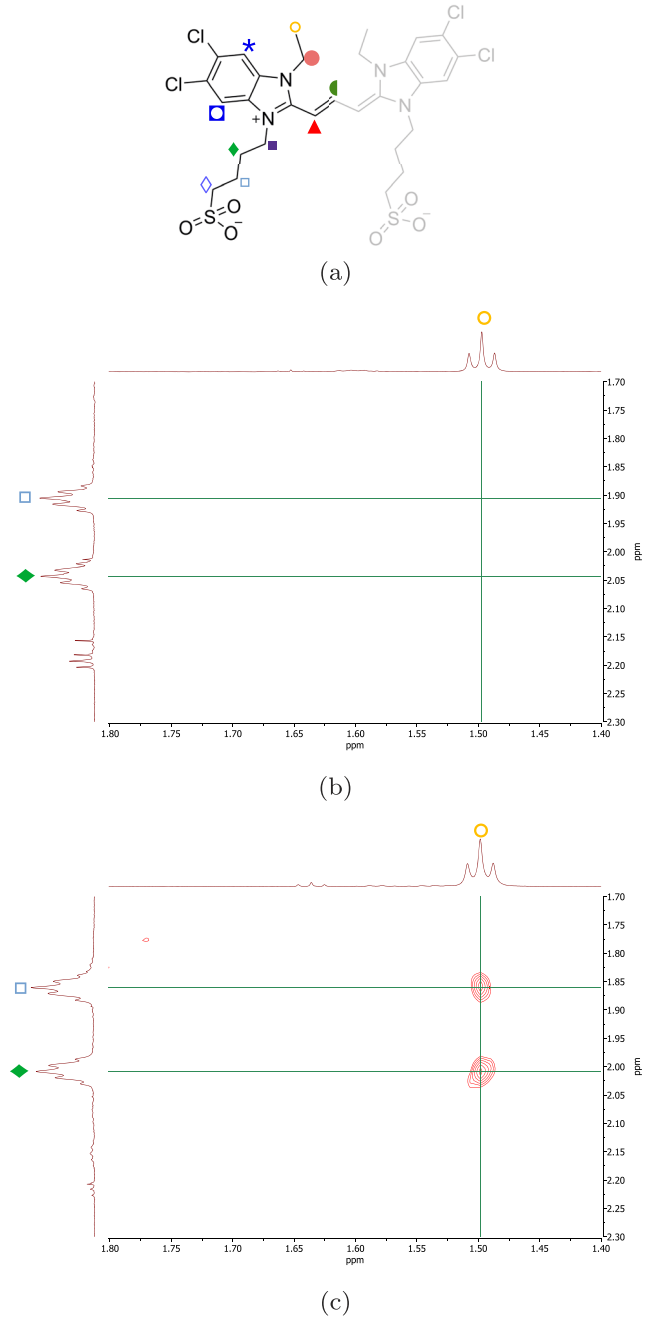


**FIG. 5.** NOESY spectrum of TDBC in the aliphatic–aliphatic region. (a) Molecular structure of TDBC, with one half highlighted. (b) NOESY spectrum of TDBC in MeOH. (c) NOESY spectrum of TDBC in 6:4 (v/v) MeOH–$H_2O$, with the appearance of cross-peaks that were not present in the monomeric TDBC.

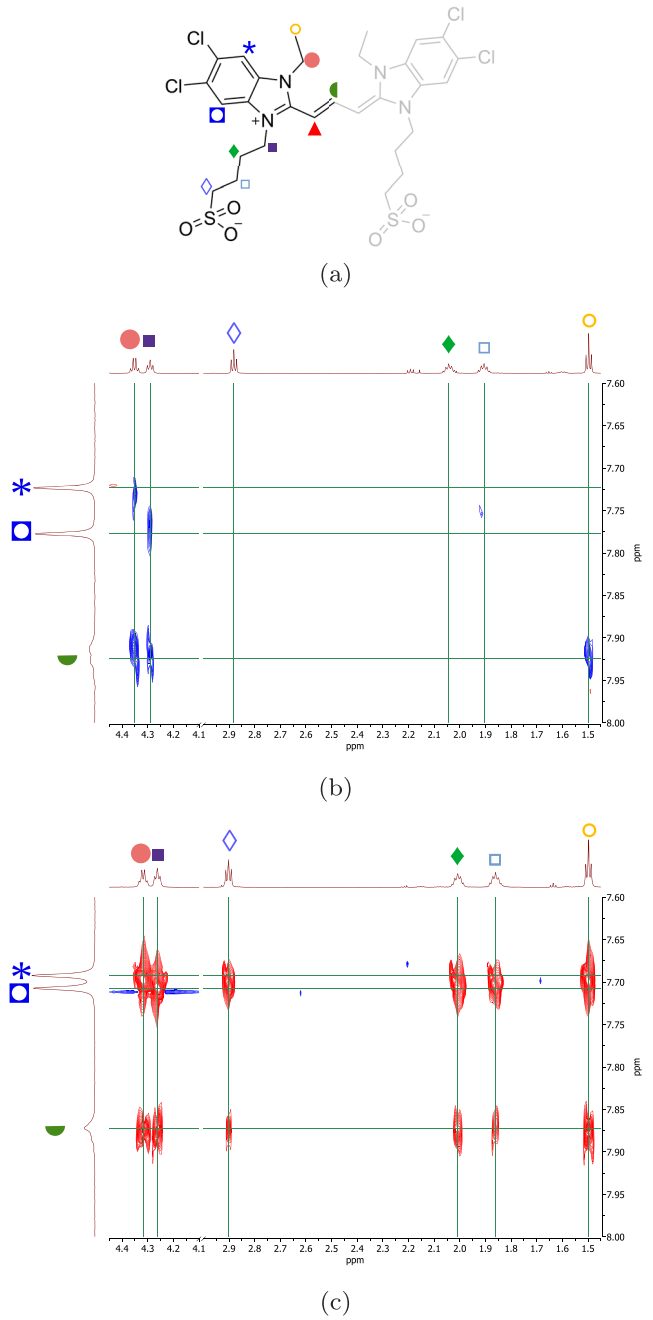


**FIG. 6.** NOESY spectrum of TDBC in the aromatic–aliphatic region. (a) Molecular structure of TDBC, with one half highlighted. (b) NOESY spectrum of TDBC in methanol. (c) NOESY spectrum of TDBC in 6:4 (v/v) MeOH–$H_2O$, with the appearance of new cross-peaks that were not present in the monomeric TDBC.

plexciton NMR data. Nevertheless, the position of the aromatic resonance is consistent with that of the J-aggregate rather than the monomer, indicating that the dye retains its aggregated character upon adsorption on the silver surface.

**Dipolar coupling in the aliphatic–aliphatic region**: Cross-peaks in a NOESY spectrum encode spatial proximity between spins, and their sign relative to a positively phased diagonal reports on the motional regime: negative for fast-tumbling molecules and positive in the slow-tumbling limit. For monomeric TDBC, the observed cross-peaks are negative, placing the molecule in the fast-tumbling regime. These cross-peaks arise strictly from intramolecular interactions, and we use them as a reference for the appearance of further peaks in the aggregate.

Upon aggregation in a $CD_3OD$:$D_2O$ mixture, the cross-peaks become positive, as expected with a transition to the slow-tumbling regime. We observe the appearance of new cross-peaks between $H_{11} \leftrightarrow H_{13}$ and $H_{11} \leftrightarrow H_{14}$, which are absent in the monomer [Fig. 5(c)]. This suggests that the short and long aliphatic chains are brought into close spatial proximity within the J-aggregate, while remaining well separated in the monomer. Such correlations are consistent with an up–down–up–down packing motif for TDBC, in which the sulfobutyl chains alternate on opposite sides of the aggregation plane. This alternating arrangement is in agreement with the structural motifs inferred from STM height measurements.[33]

**Dipolar coupling in the aromatic–aliphatic region**. When transitioning from monomer to aggregate, we observe the appearance of several cross-peaks between $H_{1,6,9}$ and $H_{11,13,14,15}$ (Fig. 6). These correlations, absent in the monomer, are also consistent with an up–down–up–down arrangement, although they present a little more ambiguity than the aliphatic–aliphatic region due to the

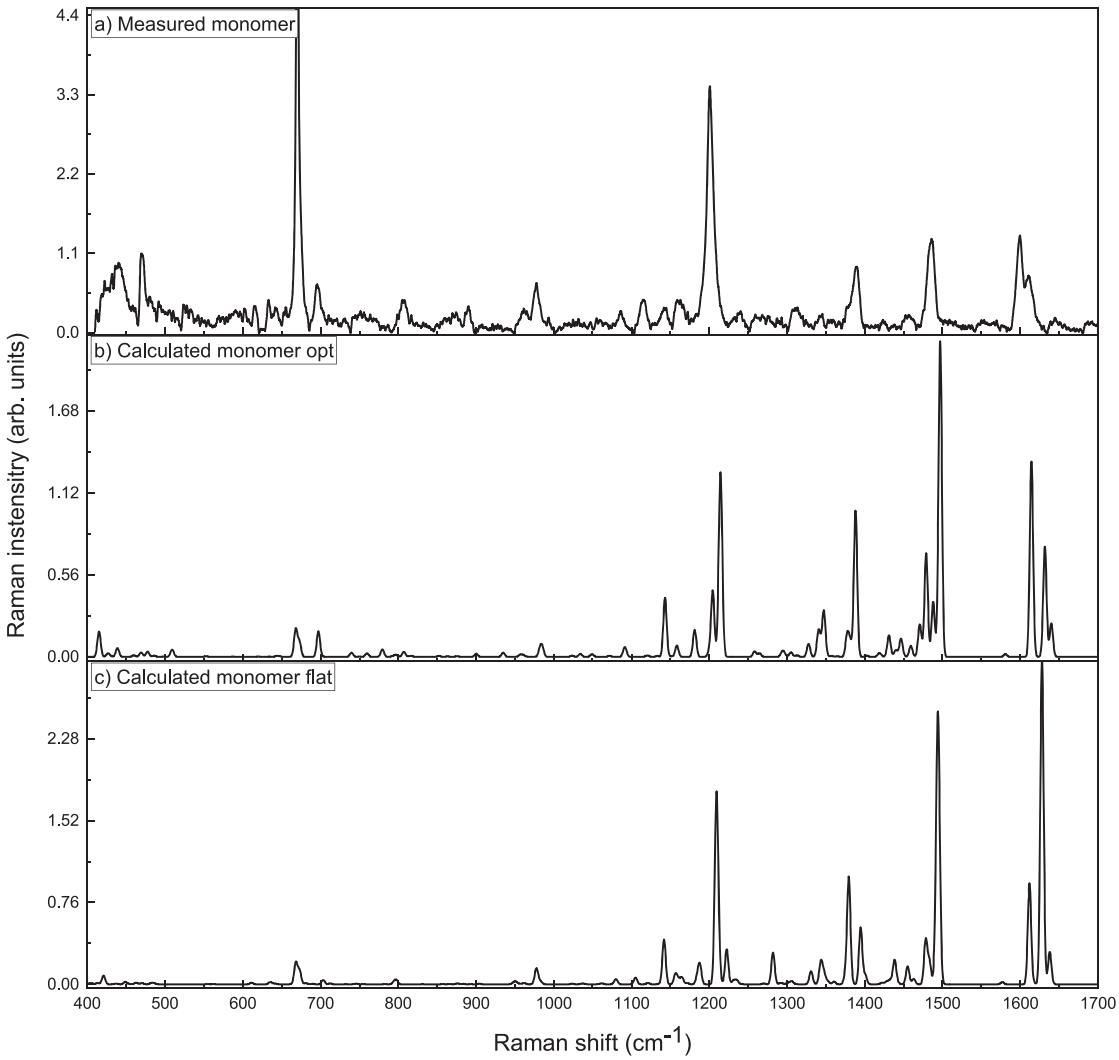


**FIG. 7.** (a) Raman spectrum of TDBC in methanol at an excitation wavelength of 577 nm at a concentration of 0.5 mg/ml. (b) Raman spectrum of the TDBC monomer in its optimized conformation with a dihedral angle of 57°. (c) Raman spectrum of the TDBC monomer with a zero dihedral angle between benzimidazole rings.

large number of couplings that appear. The aliphatic region provides stronger evidence toward the relative orientation of the individual monomers in the aggregate.

Taken together, the $^1$H and NOESY measurements establish clear conformational and packing constraints for TDBC aggregates in solution. In particular, the emergence of aliphatic–aliphatic cross-peaks absent in the monomer, combined with the inversion of NOESY cross-peak signs, provides strong evidence for large, slowly tumbling aggregates with alternating side chain orientations. These NMR-derived constraints will serve as a reference for interpreting the vibrational signatures of aggregation and adsorption discussed below.

## C. Raman

### 1. Resonance Raman

We acquired Raman spectra of TDBC monomers in methanol, J-aggregates in water, and plexcitonic assemblies in water and compared them with normal modes predicted by density functional theory (DFT) calculations. The excitation wavelength of 577 nm is resonant with the aggregate absorption band and overlaps the plexciton resonance. To assist in the assignment of the observed vibrational features, we compared the experimental spectra with DFT normal-mode calculations for representative monomeric and dimeric TDBC geometries. These calculations are used here solely for vibrational assignment; the full computational methodology and adsorption geometries are discussed in Sec. III D. Because the experimental spectra are resonance-enhanced, whereas the DFT Raman activities correspond to non-resonant Raman, we primarily use the calculations to guide mode assignment and to interpret frequency shifts and mode character, while relative intensities are discussed qualitatively (see the supplementary material for the main normal mode nuclear displacements). As reference monomer geometries, we consider two limiting cases: an optimized geometry with an inter-ring dihedral angle of 57° between the planes of the two benzimidazole rings and a planar geometry in which the two benzimidazole rings lie in the same plane. These are referred to below as the optimized and flat geometries, respectively.

**Raman of TDBC monomer in methanol**. We identify several Raman modes for TDBC in methanol in the 400–1700 cm$^{-1}$ region (Fig. 7 and Table I). The experimental spectrum is broadly consistent with the simulated spectra of the optimized monomer (twisted benzimidazole rings with bent aliphatic chains). Two bands, near 670 and 1201 cm$^{-1}$, are considerably stronger than predicted. This could arise from electronic resonance enhancement not captured by non-resonant Raman activities. The 1201 cm$^{-1}$ mode spacing is resolved in the vibronic progression of the monomer absorption spectrum, and the mode also appears in beating frequencies observed in 2D electronic spectroscopy,[17] so it is expected to have a strong resonant enhancement. In the DFT simulations, the two modes near 1598 and 1612 cm$^{-1}$ are sensitive to the dihedral angle between the benzimidazole rings: the planarized geometry yields $I_{1612} > I_{1598}$, while the optimized twisted geometry reverses this ordering.

**Raman of J-aggregates in water**. We measured the Raman spectrum of TDBC J-aggregates in water using an excitation wavelength of 577 nm and compared it with the simulated spectra obtained for a dimer structure [Fig. 8(a) and Table II]. We observe excellent agreement between measurements and simulations in the higher frequency region. However, in the lower frequency region (< 900 cm$^{-1}$), we observe that resonances appear much more intense than predicted, which is seen clearly for the 671 cm$^{-1}$ mode. This could be the result of an electronic resonance enhancement, or Aggregation-Enhanced Raman Scattering (AERS), due to many more molecules participating in the aggregate.[51,52] Discrepancies between experiments and simulations are expected given that we cannot capture the geometry of an aggregate based on a dimer structure, and simulations involving more than two interacting molecules are computationally demanding due to both the overall size of the aggregate and the conformational flexibility of each participating molecule. As shown by Coles *et al.*, different starting points for a dimer will give different optimized geometries and associated simulated Raman spectra.[34] Inspection of the atomic motions for each calculated Raman mode shows that the low frequency modes (<900 cm$^{-1}$) are delocalized over both molecules of the dimer and,

**TABLE I.** Frequencies and intensities of Raman modes calculated and measured for a TDBC monomer.

| | Calculated | | | | Experimental | |
|---|---|---|---|---|---|---|
| | Opt | | Flat | | | |
| Mode | Freq (cm) | Intensity | Freq (cm) | Intensity | Freq (cm) | Intensity |
| 1 | 1632 | 0.95 | 1628 | 3.50 | 1611 | 0.93 |
| 2 | 1615 | 1.55 | 1612 | 1.12 | 1599 | 1.54 |
| 3 | ... | ... | ... | ... | 1550 | 0.18 |
| 4 | ... | ... | ... | ... | 1523 | 0.22 |
| 5 | 1497 | 2.33 | 1494 | 2.48 | 1485 | 1.57 |
| 6 | 1446 | 0.16 | 1455 | 0.20 | 1455 | 0.22 |
| 7 | 1431 | 0.17 | ... | ... | 1425 | 0.25 |
| 8 | 1388 | 1 | 1380 | 1 | 1390 | 1 |
| 9 | 1378 | 0.24 | ... | ... | 1378 | 0.33 |
| 10 | 1347 | 0.34 | 1347 | 0.16 | ... | ... |
| 11 | 1341 | 0.22 | 1344 | 0.23 | ... | ... |
| 12 | ... | ... | 1282 | 0.27 | ... | ... |
| 13 | 1204 | 0.45 | 1209 | 1.46 | 1201 | 3.79 |
| 14 | 1159 | 0.08 | 1157 | 0.11 | 1162 | 0.48 |
| 15 | 1143 | 0.34 | 1142 | 0.33 | 1141 | 0.31 |
| 16 | ... | ... | 1105 | 0.05 | 1115 | 0.50 |
| 17 | 1091 | 0.06 | 1081 | 0.04 | 1086 | 0.25 |
| 18 | ... | ... | ... | ... | 994 | 0.22 |
| 19 | 984 | 0.07 | 978 | 0.1 | 978 | 0.52 |
| 20 | 960 | 0.01 | 962 | 0.01 | 959 | 0.4 |
| 21 | 900 | 0.01 | ... | ... | 891 | 0.41 |
| 22 | ... | ... | ... | ... | 829 | 0.27 |
| 23 | 807 | 0.03 | 797 | 0.03 | 805 | 0.34 |
| 24 | 697 | 0.09 | 703 | 0.02 | 696 | 0.66 |
| 25 | 668 | 0.1 | 669 | 0.1 | 671 | 6.88 |
| 26 | ... | ... | ... | ... | 655 | 0.28 |
| 27 | ... | ... | ... | ... | 642 | 0.51 |
| 28 | ... | ... | 635 | 0.01 | 633 | 1.05 |
| 29 | ... | ... | 611 | 0.01 | 617 | 0.61 |
| 30 | 469 | 0.01 | 478 | 0.01 | 470 | 1.77 |
| 31 | 439 | 0.02 | 449 | 0.01 | 446 | 0.88 |

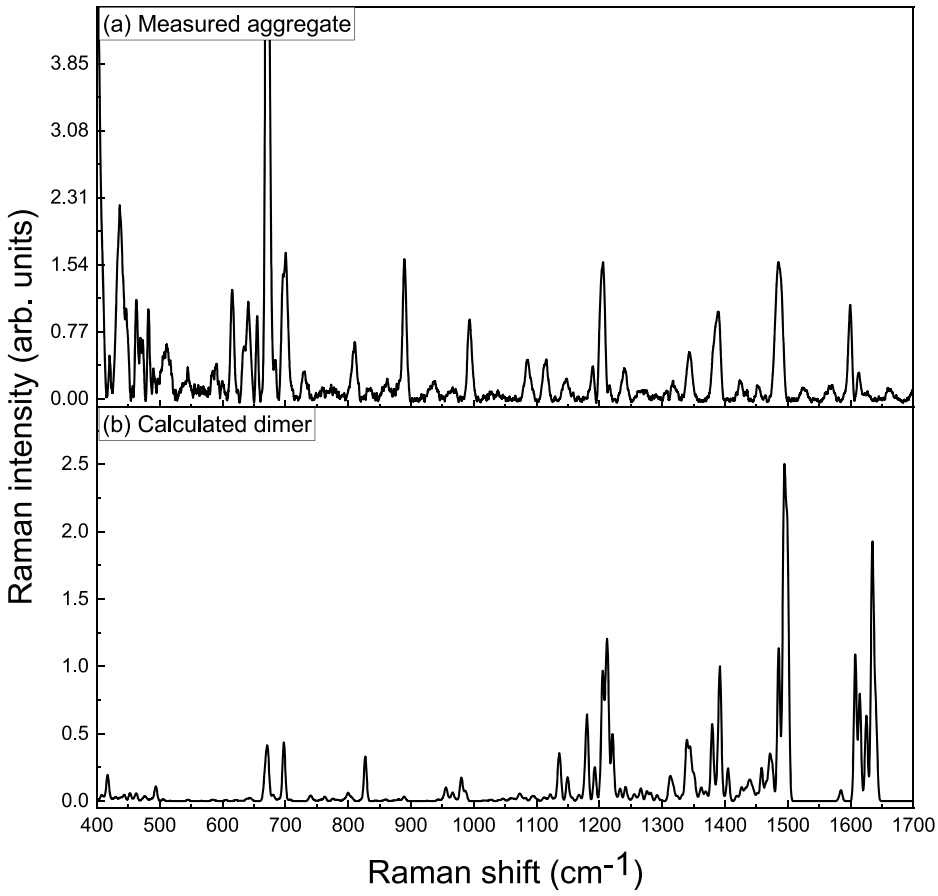


(a)

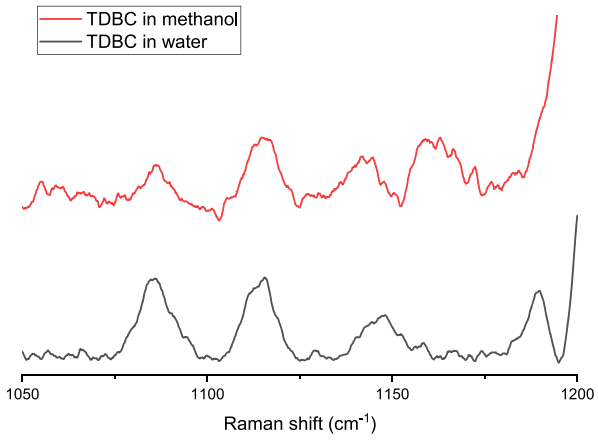


(b)

**FIG. 8.** Resonance Raman signatures of TDBC aggregation in water. (a) Raman spectrum of TDBC in water at an excitation wavelength of 577 nm compared with the dimer simulation. (b) Zoom of the 1050–1200 $cm^{-1}$ region comparing monomeric TDBC in methanol and J-aggregates in water.

**TABLE II.** Raman modes for TDBC J-aggregates in water and the Raman simulated modes for a TDBC dimer.

| | Calculated | | Experimental | |
|---|---|---|---|---|
| | Dimer | | | |
| Mode | Freq (cm) | Intensity | Freq (cm) | Intensity |
| 1 | 1634 | 2.33 | 1613 | 0.31 |
| 2 | 1608 | 1.34 | 1599 | 1.04 |
| 3 | 1585 | 0.13 | 1568 | 0.20 |
| 4 | ⋯ | ⋯ | 1526 | 0.13 |
| 5 | 1494 | 2.87 | 1486 | 1.51 |
| 6 | 1458 | 0.34 | 1452 | 0.17 |
| 7 | 1426 | 0.16 | 1424 | 0.22 |
| 8 | 1392 | 1 | 1389 | 1 |
| 9 | 1380 | 0.58 | 1381 | 0.59 |
| 10 | 1344 | 0.47 | 1344 | 0.54 |
| 11 | 1313 | 0.19 | 1317 | 0.25 |
| 12 | 1266 | 0.1 | 1266 | 0.15 |
| 13 | 1241 | 0.13 | 1240 | 0.37 |
| 14 | 1221 | 0.54 | 1216 | 0.18 |
| 15 | 1212 | 1.08 | 1205 | 1.45 |
| 16 | 1180 | 0.55 | 1189 | 0.42 |
| 17 | 1136 | 0.28 | 1147 | 0.25 |
| 18 | 1094 | 0.04 | 1114 | 0.45 |
| 19 | 1073 | 0.05 | 1086 | 0.46 |
| 20 | 980 | 0.13 | 994 | 0.90 |
| 21 | 966 | 0.06 | 966 | 0.14 |
| 22 | 889 | 0.03 | 890 | 1.53 |
| 23 | ⋯ | ⋯ | 862 | 0.23 |
| 24 | ⋯ | ⋯ | 835 | 0.12 |
| 25 | 827 | 0.19 | 810 | 0.61 |
| 26 | 740 | 0.03 | 730 | 0.37 |
| 27 | 698 | 0.21 | 700 | 1.61 |
| 28 | 680 | 0.05 | 683 | 0.49 |
| 29 | 671 | 0.2 | 671 | 19.02 |
| 30 | ⋯ | ⋯ | 655 | 0.96 |
| 31 | 643 | 0.02 | 641 | 1.09 |
| 32 | 638 | 0.01 | 634 | 0.65 |
| 33 | ⋯ | ⋯ | 615 | 1.13 |
| 34 | 584 | 0.01 | 589 | 0.45 |
| 35 | 545 | 0.01 | 545 | 0.41 |
| 36 | 476 | 0.02 | 482 | 0.98 |
| 37 | 463 | 0.02 | 463 | 1.13 |
| 38 | 443 | 0.02 | 437 | 2.07 |
| 39 | 417 | 0.06 | 420 | 0.66 |
| 40 | 407 | 0.02 | 401 | 4.17 |
| 41 | 389 | 0.02 | 387 | 0.65 |
| 42 | 374 | 0.01 | 373 | 1.42 |
| 43 | 361 | 0.03 | 355 | 1.85 |
| 44 | 331 | 0.02 | 339 | 0.58 |
| 45 | 319 | 0.02 | 324 | 5.05 |
| 46 | 315 | 0.02 | 317 | 1.97 |
| 47 | 275 | 0.03 | 274 | 0.66 |
| 48 | 221 | 0.01 | 226 | 1.43 |

thus, more susceptible to the specific aggregation geometry, while the higher frequency modes (>900 $cm^{-1}$) are localized on one of the molecules. Among the different modes that change upon aggregation, and which will be mentioned in detail below, we note now that there is a mode at 1160 $cm^{-1}$ that appears for the monomer but which is absent in the aggregate [see Fig. 8(b)]. The two modes at 1598 and 1612 $cm^{-1}$ are similar between the monomer and aggregates. Similarly, the resonances in the region 950–1010 $cm^{-1}$ show distinct signatures between TDBC in methanol and in water.

**Raman of plexcitons in water**. A comparison of the Raman spectra of plexcitons with those of the monomer and the aggregate shows shared features with each (Fig. 9 and Table III). Overall, the plexciton spectrum shares many modes with the aqueous aggregate but also retains monomer-like signatures and exhibits a small number of additional features, indicating adsorption-induced structural heterogeneity at the interface. We exclude photodegradation products by verifying the reproducibility of the spectra before and after prolonged exposure. The low intensity of the excitation laser, as well as the measurement temperature of 77 K, contributes toward sample stability. In addition, photoprotection effects have been reported in plexcitonic assemblies owing to a change in energetics that precludes the formation of oxygen singlet species.[53]

**Excitation wavelength dependence**. The excitation wavelength dependence of the plexciton Raman modes is shown in Fig. 10. The three excitation wavelengths are resonant with subsets of molecules with different electronic transition energies (for example, due to different conformations of the molecules) so that we effectively select different sub-ensembles of molecules with different geometries. In addition, exciting a plasmon with a different wavelength creates a different field configuration, enhancing the field in spatially different locations. Different Raman excitation wavelengths sample both different spatial regions and molecules with different electronic excitation transitions. It provides an indication of the heterogeneity of conformations. We observe that the spectra at excitation wavelengths of 577 and 647 nm share many similarities, with some variations in the peak intensities, which is expected from different resonance enhancements. These wavelengths are resonant with the upper and lower polariton branches, respectively, with the wavelength of 577 nm also being resonant with the J-aggregates in solution. The Raman spectrum with an excitation wavelength of 441 nm shows more marked differences, such as the appearance of new modes and frequency shifts of the existing ones. This excitation wavelength is resonant with the blue tail of the monomer electronic transition as well as the blue tail of the upper polariton branch so that we are more sensitive to any monomer species that might be present. A mode near 1160 $cm^{-1}$, which we identified as predominantly monomeric in character (Table I), appears at all excitation wavelengths, suggesting that a sub-population of unaggregated TDBC is present on the nanoparticle surface or that parts of the aggregate have distortions that bring them closer to a monomer geometry.

We also observe that with a Raman excitation wavelength of 441 nm, the spectral profile in the 1600 $cm^{-1}$ region differs from that observed with excitation wavelengths of 577 and 647 nm: the shoulder structure changes and the peak positions show a slight redshift. Since 441 nm is resonant with the upper polariton branch and

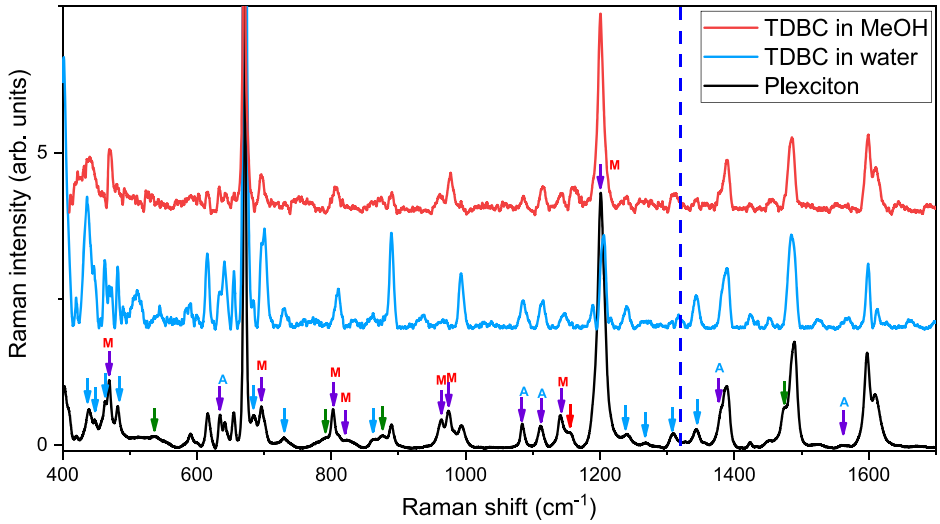


**FIG. 9.** Raman spectra of TDBC in methanol (red), TDBC in water (blue), and TDBC–Ag plexcitonic assemblies (black). The modes that change when binding to the nanoparticle are indicated by arrows. The red arrows indicate the modes that are present in the monomeric form and plexcitonic assemblies, the blue arrows indicate the modes that are present in the J-aggregate form and plexcitonic assemblies, the green arrows indicate new modes that are only seen in plexcitonic assemblies, and the purple arrows indicate modes that are present in all three species. The letters M and A denote a similarity of the mode frequency with monomer or aggregate, respectively.

the blue tail of the monomer absorption, it may selectively enhance a minority sub-population of adsorbed molecules in a distinct conformation. This assignment remains tentative but warrants further investigation if the 1598/1612 $cm^{-1}$ pair can provide information on dihedral angle distortions, as suggested by DFT simulations. In this case, it would mean a planarization of the benzimidazole rings induced by the surface, whose distorted geometry would have a higher lying absorption band resonant with 441 nm.

### 2. THz-Raman

The THz-Raman region probes low-frequency intermolecular and collective modes that are particularly sensitive to longer-range order and mesoscale packing. We measured bare Ag nanodisks, monomers, J-aggregates, and plexcitons in solution at 633 nm excitation (Fig. 11). To place the THz-Raman intensities on a common scale, we rescaled this spectral region using the intensity of the 670 $cm^{-1}$ mode measured independently at 577 nm excitation; the relative intensities shown are, therefore, directly comparable across samples.

Several resonances are observed, with two dominant features near 140 and 322 $cm^{-1}$. The 140 $cm^{-1}$ mode appears at a similar frequency in monomers and aggregates but becomes broader and develops a more asymmetric line shape in plexcitons. The 322 $cm^{-1}$ feature is particularly informative: in the aggregate, it resolves into multiple closely spaced resonances, suggestive of longer-range structural order, whereas in both the monomer and the plexciton, it appears as a single, broader band.

Taken together with the higher-frequency Raman data, this suggests a picture in which the nearest-neighbor interactions—probed by modes above 400 $cm^{-1}$—remain similar between J-aggregates and plexcitons, while the longer-range packing order—probed by the low-frequency collective modes—is disrupted upon adsorption onto the nanoparticle surface. The preservation of local aggregate structure is consistent with the similarity in bright-state transition frequencies between solution-phase J-aggregates and plexcitons.

## D. DFT

To rationalize the experimental NMR and Raman observations, we investigated several representative geometries of TDBC using density functional theory, including monomer conformers with different inter-ring dihedral angles between the two benzimidazole planes, dimer configurations as minimal models of aggregation, and surface-bound conformations on Ag. These calculations are used to identify energetically accessible geometries consistent with the spectroscopic constraints and to analyze the vibrational character of the associated normal modes (see the supplementary material for the nuclear displacements of the most prominent Raman modes).

Due to the flexibility of the monomer imparted by the aliphatic chains and the torsional degree of freedom between the two rings, we carried out a geometry optimization. We selected a geometry in which the $\pi$ system is constrained to a planar conformation (flat monomer, Fig. 12) as well as a fully optimized geometry (optimized monomer, Fig. 13) for further analysis, motivated by the sensitivity of specific Raman modes to aromatic torsion. The two geometries differ in energy by 0.251 eV, favoring the twisted conformation. The obtained optimized geometry agrees with that reported in Ref. 34. We calculate an angle of 57° between the planes of the two aromatic rings.

Dimers were constructed by aligning the molecular transition dipoles at angles consistent with J-type aggregation and subsequently optimized, following earlier work[34] (Fig. 14). We observe a curving of the aliphatic chains and an expected close intermolecular contact between $\pi$ systems again. The dimer was further stabilized by ~22 kcal/mol per monomer of TDBC relative to the isolated monomer, at the electronic structure level. The two monomers in the optimized dimer exhibit dihedral angles of ~32° and 68°, highlighting the heterogeneity of local torsions that can arise upon aggregation and that is reflected in the vibrational spectra. These dimers are very helpful in understanding the behavior during aggregation, although they have to be taken with caution when considering quantitative agreement with real aggregates given that real aggregates consist of several (usually more than 10) molecules.

**TABLE III.** Vibrational modes of TDBC in methanol, water, and plexcitons.

| Methanol | | Water | | Plexciton | |
|---|---|---|---|---|---|
| Freq ($cm^{-1}$) | Intensity | Freq ($cm^{-1}$) | Intensity | Freq ($cm^{-1}$) | Intensity |
| 1611 | 0.93 | 1613 | 0.31 | 1610 | 0.86 |
| 1599 | 1.54 | 1599 | 1.04 | 1598 | 1.58 |
| 1550 | 0.18 | 1568 | 0.20 | 1561 | ... |
| 1523 | 0.22 | 1526 | 0.13 | 1525 | 0.01 |
| 1485 | 1.57 | 1486 | 1.51 | 1489 | 1.77 |
| ... | ... | ... | ... | 1475 | 0.65 |
| 1455 | 0.22 | 1452 | 0.17 | 1453 | 0.08 |
| 1425 | 0.25 | 1424 | 0.22 | 1424 | 0.04 |
| 1390 | 1 | 1389 | 1 | 1388 | 1 |
| 1378 | 0.33 | 1381 | 0.59 | 1381 | 0.66 |
| ... | ... | 1344 | 0.54 | 1343 | 0.27 |
| ... | ... | 1317 | 0.25 | 1309 | 0.19 |
| ... | ... | 1266 | 0.15 | 1268 | 0.04 |
| ... | ... | 1240 | 0.37 | 1240 | 0.18 |
| ... | ... | 1216 | 0.18 | ... | ... |
| 1201 | 3.79 | 1205 | 1.45 | 1202 | 4.31 |
| ... | ... | 1189 | 0.42 | ... | ... |
| 1162 | 0.48 | ... | ... | 1155 | 0.21 |
| 1141 | 0.31 | 1147 | 0.25 | 1141 | 0.5 |
| 1115 | 0.50 | 1114 | 0.45 | 1112 | 0.32 |
| 1086 | 0.25 | 1086 | 0.46 | 1084 | 0.36 |
| 994 | 0.22 | 994 | 0.9 | 994 | 0.33 |
| 978 | 0.52 | 966 | 0.14 | 975 | 0.58 |
| 959 | 0.4 | ... | ... | 964 | 0.43 |
| 891 | 0.41 | 890 | 1.53 | 890 | 0.35 |
| ... | ... | ... | ... | 876 | 0.16 |
| ... | ... | 862 | 0.23 | 863 | 0.1 |
| 829 | 0.27 | 835 | 0.12 | 823 | 0.09 |
| ... | ... | ... | ... | 809 | 0.19 |
| 805 | 0.34 | 810 | 0.61 | 803 | 0.61 |
| ... | ... | ... | ... | 793 | 0.13 |
| ... | ... | 730 | 0.37 | 730 | 0.13 |
| 696 | 0.66 | 700 | 1.61 | 696 | 0.65 |
| ... | ... | 683 | 0.49 | 685 | 0.51 |
| 671 | 6.88 | 671 | 19.02 | 671 | 7.95 |
| 655 | 0.28 | 655 | 0.96 | 655 | 0.55 |
| 642 | 0.51 | 641 | 1.09 | 642 | 0.39 |
| 633 | 1.05 | 634 | 0.65 | 634 | 0.51 |
| 617 | 0.61 | 615 | 1.13 | 616 | 0.53 |
| ... | ... | 589 | 0.45 | 590 | 0.19 |
| ... | ... | 545 | 0.41 | ... | ... |
| ... | ... | ... | ... | 533 | 0.15 |
| ... | ... | ... | ... | 514 | 0.14 |
| ... | ... | 482 | 0.98 | 482 | 0.66 |
| 470 | 1.77 | 463 | 1.13 | 470 | 1.1 |
| ... | ... | ... | ... | 463 | 0.75 |
| ... | ... | ... | ... | 448 | 0.44 |
| 446 | 0.88 | 437 | 2.07 | 439 | 0.6 |
| ... | ... | 420 | 0.66 | 420 | 0.15 |
| ... | ... | ... | ... | 408 | 0.65 |
| ... | ... | 401 | 4.17 | 403 | 0.99 |
| ... | ... | 387 | 0.65 | 389 | 0.32 |

**TABLE III.** (*Continued*.)

| Methanol | | Water | | Plexciton | |
|---|---|---|---|---|---|
| Freq ($cm^{-1}$) | Intensity | Freq ($cm^{-1}$) | Intensity | Freq ($cm^{-1}$) | Intensity |
| ... | ... | 373 | 1.42 | 373 | 0.68 |
| ... | ... | ... | ... | 363 | 0.91 |
| ... | ... | 355 | 1.85 | ... | ... |
| ... | ... | 339 | 0.58 | 340 | 1.26 |
| ... | ... | 324 | 5.05 | 325 | 3.79 |
| ... | ... | 317 | 1.97 | ... | ... |
| ... | ... | 274 | 0.66 | ... | ... |
| ... | ... | 226 | 1.43 | ... | ... |

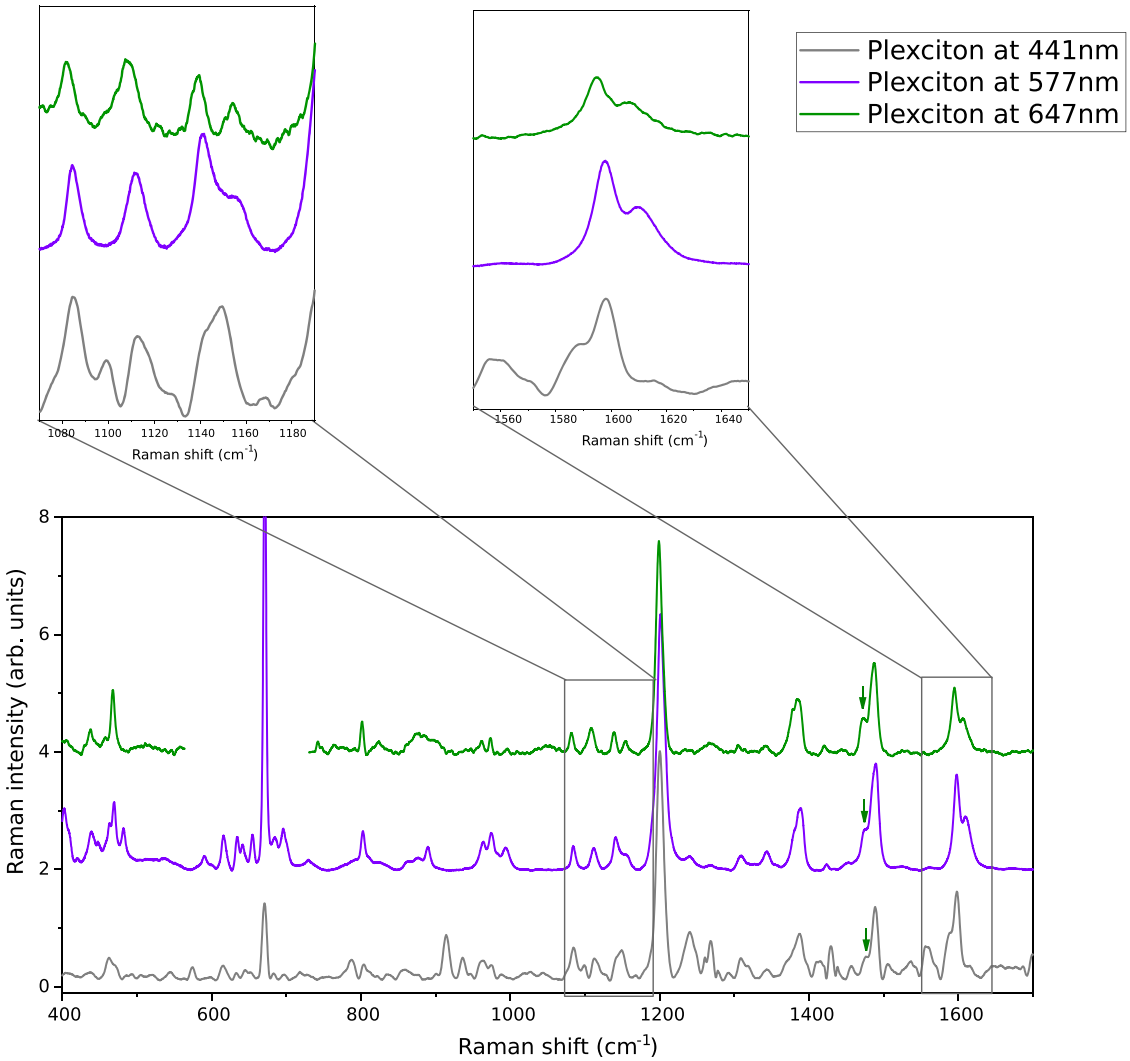


**FIG. 10.** Raman spectra of plexciton assemblies at different excitation wavelengths. The break at the 647 nm excitation wavelength is due to a parasitic satellite line of the exciting laser.

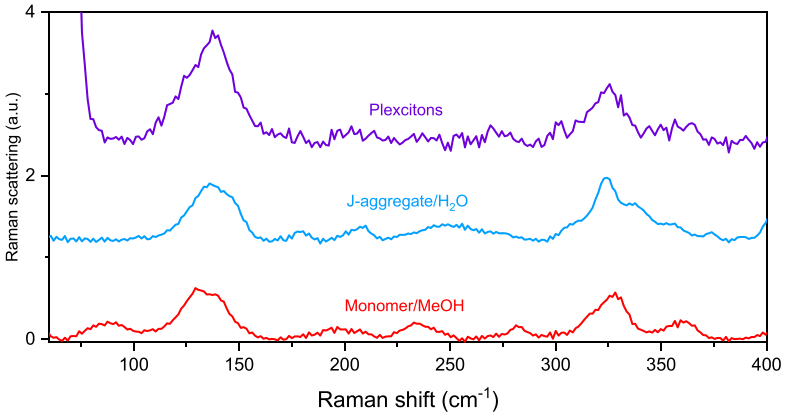


**FIG. 11.** THz-Raman spectra of TDBC monomers in methanol (red), TDBC J-aggregates in water (blue), and plexcitons (purple).

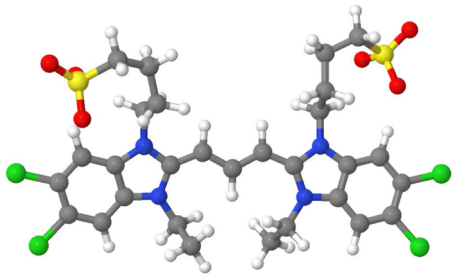

**FIG. 12.** Geometry of the TDBC monomer structure in planar conformation.

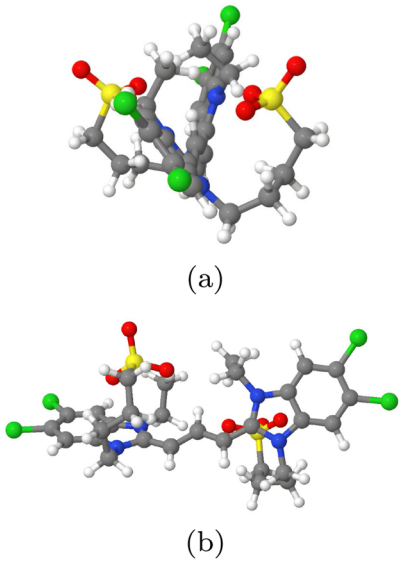


**FIG. 13.** Geometry of the TDBC monomer structure in optimized conformation. (a) Side view and (b) front view.

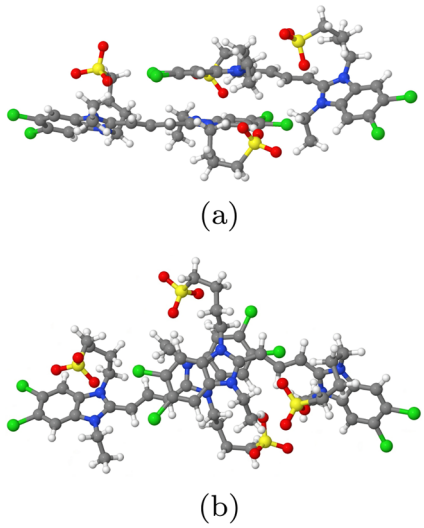


**FIG. 14.** Geometry of the TDBC dimer structure in optimized conformation. (a) Side view and (b) front view.

We also calculated the optimized geometry of TDBC on a Ag slab. The Ag slab atoms were kept fixed during all optimizations. In the first calculation, the molecule was constrained to a flat geometry [Fig. 15(a)], while for the second we allowed a full geometry optimization of the molecule [Fig. 15(b)]. In both scenarios, the preferred anchoring groups were the sulfonate groups via two bridging oxygen atoms. When the molecule was free to move, the most energetically favorable configuration had the aromatic ring parallel to the surface.

Normal modes were calculated for the monomeric and dimeric geometries and classified according to their dominant atomic motions (out-of-plane, in-plane, and aliphatic chain) and spatial extent (localized on a single molecule or delocalized across two molecules). This classification provides the basis for interpreting aggregation- and adsorption-sensitive features in the Raman and THz-Raman spectra (see the supplementary material).

Taken together, the DFT results establish a hierarchy of energetically accessible TDBC geometries that are consistent with the experimental constraints. The monomer exhibits a preferred twisted conformation, aggregation introduces heterogeneous torsional environments even at the dimer level, and adsorption on Ag favors planarization of the aromatic core via sulfonate binding. These

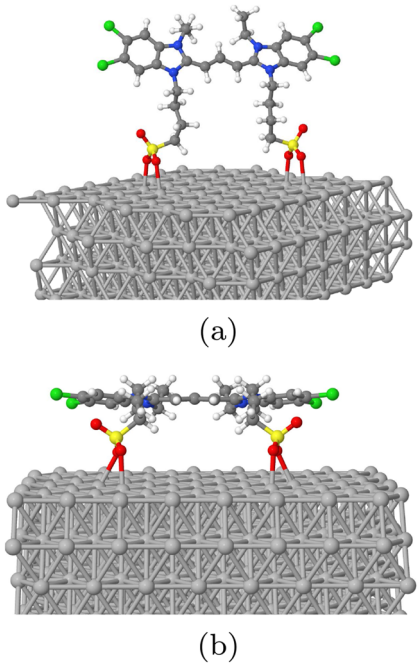


**FIG. 15.** Geometry of TDBC on a Ag surface. (a) Molecule fully optimized and (b) molecule in the flat position.

trends provide a microscopic framework for interpreting the coexistence of aggregate-like and monomer-like vibrational signatures observed in plexcitonic assemblies.

## IV. DISCUSSION

Below, we first discuss the geometry of TDBC J-aggregates in solution, then analyze how vibrational fingerprints reflect aggregation and disorder, and finally consider the most likely interfacial structures and their implications for plexciton design.

Our combined NMR, Raman, THz-Raman, and DFT study provides new insights into the structural organization of TDBC molecules in their monomeric, aggregated, and plexcitonic states. The main outcome is that while plexcitons retain many of the spectroscopic signatures of J-aggregates in water, their interfacial environment with Ag nanodisks introduces additional structural heterogeneity: the long-range collective order characteristic of solution-phase aggregates is disrupted, and vibrational signatures characteristic of monomeric or weakly aggregated TDBC emerge alongside the dominant aggregate-like modes. Whether these monomer-like signatures arise from isolated molecules adsorbed directly on the Ag surface, from molecules at the edges of finite aggregate domains, or from adsorption-induced distortions that locally break aggregate symmetry cannot be determined from the present data. In addition to constraining the geometry of TDBC in its various environments, we identify spectroscopic markers that can serve as practical diagnostics for monitoring the aggregation state and adsorption geometry of similar cyanine dyes.

**Geometry of TDBC J-aggregates**. STM and fluorescence microscopy studies have established that cyanine and carbocyanine dyes adopt several packing motifs, including staircase, ladder, brickwork, and tubular arrangements.[54,55] For TDBC, two-dimensional sheet-like J-aggregates are the predominant structure in aqueous solution. However, NMR characterization of these aggregates in pure water is precluded by the extreme line broadening that accompanies the formation of large, slowly tumbling species. By dissolving TDBC in a deuterated 6:4 (v/v) methanol–water mixture, we restrict the aggregate size sufficiently to recover resolved $^{1}$H resonances while maintaining aggregation. Optical absorption under these conditions confirms that aggregation is achieved. This mixed-solvent strategy provides direct NMR access to aggregate packing geometry that is otherwise inaccessible and is, in principle, transferable to other J-aggregate-forming cyanine dyes.

The resulting NOESY spectra reveal intermolecular cross-peaks—notably between $H_{11}$ and $H_{13,14}$—that are absent in the monomer and are most naturally compatible with an alternating, symmetric arrangement of sulfobutyl side chains on opposite sides of the aggregation plane. This arrangement is consistent with the brickwork packing motif, although the present data do not allow us to distinguish among the different two-dimensional packing geometries. We propose these cross-peaks as a diagnostic indicator of the up–down alternating motif. Whereas STM height measurements infer the relative chain orientation indirectly from the overall layer thickness,[33] the NOESY cross-peaks provide a more direct probe, reporting on spatial proximity between specific nuclei on neighboring molecules within the aggregate. Because these constraints are complementary to the electronic and vibrational probes typically used for these systems, the mixed-solvent NMR approach presented here may offer a general route to characterizing intermolecular packing in J-aggregate-forming cyanine dyes.

Two alternative explanations of the newly observed NOESY correlations are changes in aliphatic side chain conformation and solvent-viscosity effects. DFT optimization of the monomer predicts a curving of both aliphatic chains toward the same face of the aromatic system, raising the question of whether further conformational changes could bring $H_{11}$ and $H_{13,14}$ within the NOESY detection limit. Although a large change in the inter-ring dihedral angle could in principle reduce the $H_{11}$–$H_{13,14}$ distance, such a distortion would simultaneously bring numerous other proton pairs into close proximity, producing a broad set of new cross-peaks that are not observed. The selectivity of the newly appearing contacts argues against a monomer conformational origin. Solvent-viscosity effects also warrant consideration. Because the rotational correlation time scales linearly with viscosity (Stokes–Einstein–Debye), the increase in viscosity upon going from methanol to the 6:4 methanol–water mixture could also push the system over the NOE sign-crossover threshold. However, we would then not expect to see the emergence of the observed cross-peaks. These arguments support the assignment of the resonances in water-methanol mixtures to J-aggregates.

**Raman spectroscopic fingerprints of aggregation**. DFT analysis of the dimer (Fig. 14) shows that low-frequency Raman modes (below 900 cm$^{-1}$) are delocalized across both molecules of the dimer unit, while higher-frequency modes (above 900 cm$^{-1}$) are localized on individual chromophores. This distinction provides a framework for interpreting the spectral changes upon aggregation and surface binding. In J-aggregates, the delocalized low-frequency modes exhibit pronounced intensity enhancements (Table II),

consistent with earlier reports of aggregation-enhanced Raman scattering (AERS) in which collective out-of-plane modes are selectively amplified.[34] We confirm the strong enhancement of the mode reported at 673 $cm^{-1}$ by Coles *et al.*, which we observe at 671 $cm^{-1}$. We observe the emergence of a cluster of modes in J-aggregates that are absent in the monomer (683 and 730 $cm^{-1}$ in the low-frequency region; a well-defined resonance at 1189 $cm^{-1}$; resonances at 1240 and 1266 and a more intense resonance at 1344 $cm^{-1}$; and new resonances at 1526 and 1568 at higher frequencies; Table II), all of which are also present in the plexciton spectrum. We, however, also observe modes in the region of >900 $cm^{-1}$ that are shared between the monomer and the plexciton but not the aggregate, such as the modes at 978 and 1160 $cm^{-1}$. Overall, we see more unique modes to plexcitonic assemblies and J-aggregates with water <900 $cm^{-1}$, while unique modes to the monomer and plexcitons appear >900 $cm^{-1}$. Nearest-neighbor packing, which governs the collective low-frequency vibrations, is preserved when the aggregate adsorbs on the Ag surface, whereas the higher-frequency modes, being sensitive to the local environment of individual chromophores, reflect the increased structural heterogeneity at the metal interface. In the THz-Raman region (below 400 $cm^{-1}$, Fig. 11), aggregates display sharper, better-resolved resonances than the monomer, consistent with the establishment of long-range periodic order. The broadening and reshaping of these features in plexcitons indicates that surface binding disrupts this longer-range periodicity while leaving short-range intermolecular interactions largely intact.

**Inferred interfacial structure of TDBC on Ag**. Several independent lines of evidence constrain the interfacial geometry of TDBC on the Ag nanodisk surface. DFT calculations show that adsorption proceeds preferentially through the sulfonate groups via two bridging oxygen atoms and that unconstrained optimization favors a planar orientation of the aromatic core parallel to the metal surface. The NOESY-derived constraint of alternating sulfobutyl chain orientation, established for aggregates in solution, is consistent with the preservation of aggregate-like collective Raman modes below 900 $cm^{-1}$ in plexcitons, indicating that nearest-neighbor packing is maintained upon adsorption. The recovery of monomer-like spectral character above 900 $cm^{-1}$ hints at a localized distortion most likely due to surface binding, while the broadening of THz-Raman features below 400 $cm^{-1}$ indicates a loss of long-range two-dimensional periodicity. The preservation of the aggregate absorption band frequency, evident from the splitting minimum in the optical absorption spectrum, further supports a geometry in which the $\pi$–$\pi$ stacking interactions that govern the J-aggregate excitonic structure remain largely intact. Taken together, these observations point toward the configuration shown in Fig. 16 as the dominant motif: small aggregated domains with preserved nearest-neighbor geometry and alternating sulfobutyl chains, anchored to the Ag surface through sulfonate bridges but lacking the extended periodic order of free-standing J-aggregates in solution. A minority population of surface-bound monomers, or possibly molecules at the edge of the aggregate, exhibits a distortion identifiable through monomer-like, high frequency modes.

**Comparison with encapsulated TDBC**. Silica encapsulation of TDBC J-aggregates has recently been shown to freeze the brickwork geometry into rigid, defect-suppressed sheets, yielding near-unity quantum yields and exceptional photostability.[33,35] Our plexciton system presents the opposite limit: attachment to a metallic surface preserves nearest-neighbor packing but introduces structural heterogeneity, breaking the long-range two-dimensional order and admitting a minority population of surface-bound monomers (Figs. 10 and 11). This contrast highlights how the same molecular scaffold responds to confining (silica) vs adsorbing (metal) interfaces: encapsulation suppresses disorder and enhances emissive performance, while metallic binding maintains strong exciton–plasmon coupling at the cost of structural uniformity. The plexciton system, therefore, occupies a regime in which hybridized light–matter states coexist with significant local geometric disorder.

**Implications for plexciton design**. Taken together, our results emphasize the complexity and heterogeneity of dye conformation on the surface of plasmonic nanoparticles. Given that the energetics are strongly tied to the aggregate order, the performance of plexcitons and their excited states is directly determined by nanoscale geometry and the degree of structural disorder at the interface. The vibrational fingerprints identified here provide practical diagnostics to keep track of this structural richness during different plexciton syntheses and eventually correlate it to function, or excited-state dynamics. We have also hinted at some possibly more detailed

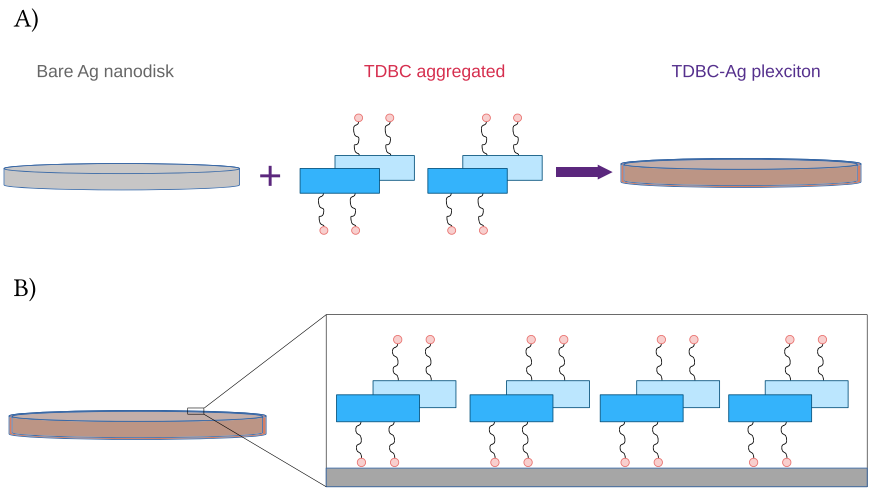


**FIG. 16.** Inferred structure of TDBC on the Ag surface of the plasmonic nanodisks. (a) Plexcitonic assembly consisting of Ag nanodisks and TDBC J-aggregates with alternating sulfonate groups above and below the aggregation please. (b) The TDBC J-aggregate structure preserves the up-down alternation of the sulfobutyl groups.

proxies of geometry, such as the torsionally sensitive intensity ratios of the $I_{1598}/I_{1612}$ mode pair that will have to be further investigated.

From a theoretical perspective, the coexistence of aggregate-like and monomer-like geometries at the metal interface implies a distribution of excitonic energies and coupling strengths within the plexcitonic assembly. The structural heterogeneity identified here provides microscopic context for models that treat plexcitons as disordered, open quantum systems with non-uniform light–matter coupling[56] and suggests that ensemble-averaged spectroscopic observables may mask significant site-to-site variation in the underlying exciton–plasmon interaction.

## V. CONCLUSION

Plexcitonic assemblies are promising platforms for the implementation of hybrid light–matter states in close contact with a chemical environment. Knowledge of the structure and its disorder is crucial to inform synthetic efforts toward better materials, as well as to build better theoretical models to describe them. Through NMR and Raman spectroscopy supported by calculations, we have identified that in TDBC aggregates, the sulfobutyl chains alternate above and below the aggregation plane, with sulfonate termini; in particular, the $H_{11} \leftrightarrow H_{13,14}$ NOESY cross-peaks serve as a direct NMR signature of this up–down alternating motif. In plexcitons, this structure is preserved, although we observe the absence of long-range order as well as the existence of monomer-like Raman modes. In this investigation, we have identified key spectroscopic fingerprints of the different molecular environments, providing a benchmark for the synthesis of more complex plexcitons as well as establishing a framework for explaining the photophysics of TDBC–Ag model systems.

## SUPPLEMENTARY MATERIAL

The supplementary material includes additional experimental details, supplementary Raman and THz-Raman spectra, extended NMR data, and nuclear mode displacements of the most prominent Raman modes obtained from DFT.

## ACKNOWLEDGMENTS

We thank Dr. Beatriz Quiroz García and Dr. Martha Elena García Aguilera for technical assistance during the NMR experiments and Tomás Rocha-Rinza for useful discussions. D.F.-S. acknowledges grant ECOS-CONAHCYT No. 321169, as well as funding from DGAPA-PAPIIT IA207223. M.J.L.-P. acknowledges the funding from CEA-Saclay and the ANR. The work of Y.A.G.J. was supported by the UNAM Postdoctoral Program (POSDOC). G.P. acknowledges the support from DGAPA-PAPIIT IN104325. J.B.-G. acknowledges a doctoral fellowship from SECIHTI. J.H.S. acknowledges the support from the Energy Area of Advance at Chalmers University of Technology. This work benefited from the Resonance Raman platforms of I2BC, supported by the French Infrastructure for Integrated Structural Biology (FRISBI, ANR-10-INSB-05) and the ECOS-Nord program (Action M21P02). We acknowledge the use of the 700 MHz NMR instrument at the LURMN national laboratory. Computations were performed at NSC Tetralith, provided by the National Academic Infrastructure for Supercomputing in Sweden (NAISS), partly funded by the Swedish Research Council (Grant No. 2022-06725).

## AUTHOR DECLARATIONS

### Conflict of Interest

The authors have no conflicts to disclose.

### Author Contributions

**J. Baños-Gutiérrez**: Formal analysis (lead); Investigation (lead); Writing – original draft (supporting); Writing – review & editing (equal). **R. Bercy**: Investigation (supporting). **Y. García Jomaso**: Investigation (supporting); Writing – review & editing (supporting). **S. Balci**: Investigation (supporting); Methodology (supporting); Supervision (supporting); Writing – review & editing (supporting). **G. Pirruccio**: Funding acquisition (equal); Investigation (equal); Supervision (supporting); Writing – review & editing (equal). **J. Halldin Stenlid**: Funding acquisition (equal); Investigation (equal); Software (lead); Writing – review & editing (equal). **M. J. Llansola-Portoles**: Conceptualization (supporting); Funding acquisition (equal); Investigation (equal); Supervision (equal); Writing – review & editing (equal). **D. Finkelstein-Shapiro**: Conceptualization (lead); Formal analysis (equal); Funding acquisition (equal); Investigation (equal); Methodology (equal); Project administration (equal); Supervision (lead); Writing – original draft (lead).

## DATA AVAILABILITY

The data that support the findings of this study are available from the corresponding author upon reasonable request.

## REFERENCES

[1] M. Hertzog, M. Wang, J. Mony, and K. Börjesson, Chem. Soc. Rev. **48**, 937 (2019).
[2] A. P. Manuel, A. Kirkey, N. Mahdi, and K. Shankar, J. Mater. Chem. C **7**, 1821 (2019).
[3] O. Bitton and G. Haran, Acc. Chem. Res. **55**, 1659 (2022).
[4] N. Peruffo, M. Bruschi, B. Fresch, F. Mancin, and E. Collini, Langmuir **39**, 12793 (2023).
[5] O. Bitton, S. N. Gupta, and G. Haran, Nanophotonics **8**, 559 (2019).
[6] P. Törmä and W. L. Barnes, Rep. Prog. Phys. **78**, 013901 (2015).
[7] G. Zengin, M. Wersaell, S. Nilsson, T. J. Antosiewicz, M. Kaell, and T. Shegai, Phys. Rev. Lett. **114**, 157401 (2015).
[8] X. Zhong, T. Chervy, S. Wang, J. George, A. Thomas, J. A. Hutchison, E. Devaux, C. Genet, and T. W. Ebbesen, Angew. Chem., Int. Ed. **55**, 6202 (2016).
[9] J. Schachenmayer, C. Genes, E. Tignone, and G. Pupillo, Phys. Rev. Lett. **114**, 196403 (2015).
[10] J. Feist and F. J. Garcia-Vidal, Phys. Rev. Lett. **114**, 196402 (2015).
[11] G. Engelhardt and J. Cao, Phys. Rev. B **105**, 064205 (2022).
[12] S. Kéna-Cohen and S. R. Forrest, Nat. Photonics **4**, 371 (2010).
[13] L. A. Martínez-Martínez, R. F. Ribeiro, J. Campos-González-Angulo, and J. Yuen-Zhou, ACS Photonics **5**, 167 (2018).
[14] R. F. Ribeiro, L. A. Martínez-Martínez, M. Du, J. Campos-González-Angulo, and J. Yuen-Zhou, Chem. Sci. **9**, 6325 (2018).
[15] B. Xiang and W. Xiong, Chem. Rev. **124**, 2512 (2024).
[16] J. Yuen-Zhou, N. Giebink, and R. Ribeiro, *Polariton Chemistry: Molecules in Cavities* (Wiley, 2025).
[17] D. Finkelstein-Shapiro, P.-A. Mante, S. Sarisozen, L. Wittenbecher, I. Minda, S. Balci, T. Pullerits, and D. Zigmantas, Chem **7**, 1092 (2021).

[18]S. Balci, B. Kucukoz, O. Balci, A. Karatay, C. Kocabas, and G. Yaglioglu, ACS Photonics **3**, 2010 (2016).
[19]N. Peruffo, F. Mancin, and E. Collini, J. Phys. Chem. C **125**, 19897 (2021).
[20]N. Peruffo, G. Parolin, E. Collini, S. Corni, and F. Mancin, Nanomaterials **12**, 1180 (2022).
[21]F. M. Balci, S. Sarisozen, N. Polat, and S. Balci, J. Phys. Chem. C **123**, 26571 (2019).
[22]A. B. Yankovich, B. Munkhbat, D. G. Baranov, J. Cuadra, E. Olsén, H. Lourenço-Martins, L. H. G. Tizei, M. Kociak, E. Olsson, and T. Shegai, Nano Lett. **19**, 8171 (2019).
[23]K. Sun, M. Du, and J. Yuen-Zhou, J. Phys. Chem. C **129**, 9837 (2025).
[24]A. Schirato, M. Maiuri, G. Cerullo, and G. Della Valle, Nanophotonics **12**, 1 (2023).
[25]B. Rousseaux, D. G. Baranov, T. J. Antosiewicz, T. Shegai, and G. Johansson, Phys. Rev. Res. **2**, 033056 (2020).
[26]P. Vasa, W. Wang, R. Pomraenke, M. Lammers, M. Maiuri, C. Manzoni, G. Cerullo, and C. Lienau, Nat. Photonics **7**, 128 (2013).
[27]A. P. Deshmukh, N. Geue, N. C. Bradbury, T. L. Atallah, C. Chuang, M. Pengshung, J. Cao, E. M. Sletten, D. Neuhauser, and J. R. Caram, Chem. Phys. Rev. **3**, 021401 (2022).
[28]N. J. Hestand and F. C. Spano, Chem. Rev. **118**, 7069 (2018).
[29]S. Ma, S. Du, G. Pan, S. Dai, B. Xu, and W. Tian, Aggregate **2**, e96 (2021).
[30]A. P. Deshmukh, A. D. Bailey, L. S. Forte, X. Shen, N. Geue, E. M. Sletten, and J. R. Caram, J. Phys. Chem. Lett. **11**, 8026 (2020).
[31]S. B. Anantharaman, K. Jo, and D. Jariwala, ACS Nano **15**, 12628 (2021).
[32]A. G. Dijkstra, H.-G. Duan, J. Knoester, K. A. Nelson, and J. Cao, J. Chem. Phys. **144**, 134310 (2016).
[33]D. H. Thanippuli Arachchi, U. Barotov, C. F. Perkinson, T. Šverko, A. E. K. Kaplan, and M. G. Bawendi, ACS Nano **18**, 20422 (2024).
[34]D. M. Coles, A. J. H. M. Meijer, W. C. Tsoi, M. D. B. Charlton, J.-S. Kim, and D. G. Lidzey, J. Phys. Chem. A **114**, 11920 (2010).
[35]U. Barotov, D. H. Thanippuli Arachchi, M. D. Klein, J. Zhang, T. Šverko, and M. G. Bawendi, Adv. Opt. Mater. **10**, 2201471 (2022).
[36]S. Balci, Opt. Lett. **38**, 4498 (2013).
[37]M. J. Frisch, G. W. Trucks, H. B. Schlegel, G. E. Scuseria, M. A. Robb, J. R. Cheeseman, G. Scalmani, V. Barone, G. A. Petersson, H. Nakatsuji, X. Li, M. Caricato, A. V. Marenich, J. Bloino, B. G. Janesko, R. Gomperts, B. Mennucci, H. P. Hratchian, J. V. Ortiz, A. F. Izmaylov, J. L. Sonnenberg, D. Williams-Young, F. Ding, F. Lipparini, F. Egidi, J. Goings, B. Peng, A. Petrone, T. Henderson, D. Ranasinghe, V. G. Zakrzewski, J. Gao, N. Rega, G. Zheng, W. Liang, M. Hada, M. Ehara, K. Toyota, R. Fukuda, J. Hasegawa, M. Ishida, T. Nakajima, Y. Honda, O. Kitao, H. Nakai, T. Vreven, K. Throssell, J. A. J. Montgomery, J. E. Peralta, F. Ogliaro, M. J. Bearpark, J. J. Heyd, E. N. Brothers, K. N. Kudin, V. N. Staroverov, T. A. Keith, R. Kobayashi, J. Normand, K. Raghavachari, A. P. Rendell, J. C. Burant, S. S. Iyengar, J. Tomasi, M. Cossi, J. M. Millam, M. Klene, C. Adamo, R. Cammi, J. W. Ochterski, R. L. Martin, K. Morokuma, O. Farkas, J. B. Foresman, and D. J. Fox, *Gaussian 16, Revision B.01*, Gaussian, Inc., Wallingford, CT, 2016.
[38]A. D. Becke, J. Chem. Phys. **98**, 5648 (1993).
[39]C. Lee, W. Yang, and R. G. Parr, Phys. Rev. B **37**, 785 (1988).
[40]F. Weigend and R. Ahlrichs, Phys. Chem. Chem. Phys. **7**, 3297 (2005).
[41]F. Weigend, Phys. Chem. Chem. Phys. **8**, 1057 (2006).
[42]S. Grimme, J. Antony, S. Ehrlich, and H. Krieg, J. Chem. Phys. **132**, 154104 (2010).
[43]S. Grimme, S. Ehrlich, and L. Goerigk, J. Comput. Chem. **32**, 1456 (2011).
[44]G. Kresse and J. Hafner, Phys. Rev. B **47**, 558 (1993).
[45]G. Kresse and J. Furthmüller, Phys. Rev. B **54**, 11169 (1996).
[46]G. Kresse and J. Furthmüller, Comput. Mater. Sci. **6**, 15 (1996).
[47]B. Hammer, L. B. Hansen, and J. K. Nørskov, Phys. Rev. B **59**, 7413 (1999).
[48]H. Aviv and Y. R. Tischler, J. Lumin. **158**, 376 (2015).
[49]J. Kowalewski and L. Mäler, *Nuclear Spin Relaxation in Liquids: Theory, Experiments, and Applications*, *Series in Chemical Physics* (CRC Press, Boca Raton, FL, 2006).
[50]D. Kruk, *Spin Relaxation* (Royal Society of Chemistry, 2022).
[51]D. L. Akins, Nanomater. Nanotechnol. **4**, 4 (2013).
[52]D. L. Akins, J. W. Macklin, L. A. Parker, and H.-R. Zhu, Chem. Phys. Lett. **169**, 564 (1990).
[53]B. Munkhbat, M. Wersäll, D. G. Baranov, T. J. Antosiewicz, and T. Shegai, Sci. Adv. **4**, eaas9552 (2018).
[54]V. V. Prokhorov, O. M. Perelygina, E. I. Mal'tsev, and A. V. Vannikov, Crystallogr. Rep. **59**, 821 (2014).
[55]V. V. Prokhorov, O. M. Perelygina, S. I. Pozin, E. I. Maltsev, and A. V. Vannikov, J. Phys. Chem. B **119**, 15168 (2015).
[56]D. Finkelstein-Shapiro, P.-A. Mante, S. Balci, D. Zigmantas, and T. Pullerits, J. Chem. Phys. **158**, 104104 (2023).